

Laser surface treatment of aluminum based composite mixed with B₄C particles



B.S. Yilbas^a, C. Karatas^b, Halil Karakoc^c, B.J. Abdul Aleem^a, S. Khan^a, N. Al-Aqeeli^{a,*}

^a Mechanical Engineering Department, KFUPM, Dhahran 31261, Saudi Arabia

^b Engineering Faculty, Hacettepe Universitesi, Ankara, Turkey

^c Faculty of Technology, Hacettepe Universitesi, Ankara, Turkey

ARTICLE INFO

Article history:

Received 29 May 2014

Received in revised form

5 July 2014

Accepted 7 August 2014

Available online 19 September 2014

Keywords:

Laser aluminum alloy

Boron carbide

Hydrophobicity

ABSTRACT

Laser treatment of hot pressed mixture of aluminum (85 wt%) and B₄C (15 wt%) is carried out. Metallurgical and morphological changes at the laser treated surface are examined using the analytical tools. Microhardness and fracture toughness of the workpiece surfaces are determined prior to and after the laser treatment process. Texture and hydrophobicity of the laser treated surface is assessed incorporating the atomic force microscopy and contact angle measurements. It is found that a dense layer consisting of fine grains of sub-micron sizes (0.8–0.4 μm) and B₄C particles is formed at the laser treated surface. Microhardness increases at the laser treated surface because of the presence of the dense layer and the formation of AlN compounds at the surface. Fracture toughness of the laser treated surface reduces slightly because of the microhardness enhancement at the surface. The textures of the laser treated surface compose of micro/nano poles, which result in higher contact angles than that of the untreated surface, and formation of AlN compound adds to the surface hydrophobicity enhancements.

© 2014 Elsevier Ltd. All rights reserved.

1. Introduction

Aluminum alloys are widely used in industry due to their low density despite their low tribological properties at the surface. However, further improvement of tribological properties is necessary to extend the life span of the parts made from aluminum, particularly, for wear applications. Although the blend of hard particles in the alloy improves the surface properties [1], because of the large differences in mechanical and thermal properties between the alloy and the hard particles limit the practical applications of the parts produced from the blend of aluminum alloy and hard particles [2]. Laser surface treatment is one of the techniques, which can be electively used to improve tribological properties of the alloy surface. In addition, it provides advantages over the conventional treatment methods despite low absorption coefficient of the aluminum alloy surface. Some of these advantages include precision of operation, fast processing time, local treatment, and low cost [3]. Laser controlled melting process provides thermal integration of the hard particles and aluminum in the mixture composite, which in turn further improves tribological properties of the composite. However, high cooling rates and shallow treatment layer result in the development of high stress levels in the laser treated layer. Although high residual

stress contributes to microhardness improvement, it has an adverse effect on the fracture toughness of the surface. In addition, high stress levels can cause asperities such as micro-cracks and crack networks at the laser treated surface. Laser surface treatment changes the texture of the surface while influencing the wetting characteristics. In this case, hydrophobicity of the surface can be modified after the laser treatment process. Consequently, investigation of the surface characteristics of the laser treated aluminum based composite blended with the hard particles becomes essential.

Considerable research studies were carried out to examine laser treatment of aluminum alloys [3–11]. Some of the research studies were focused on structural and mechanical characteristics of the laser treated aluminum alloys [3–7]. Structural changes in the laser cladded aluminum alloy surface were examined by Pokhmurs'ka [3]. He showed that the melting started for relatively low intensities of laser beams at the interface of the alloy and the melting propagated towards the bulk of the alloy as the heating period progressed. As the intensity of laser irradiation increased, the melting started from the surface and the thickness of the re-melted and recrystallized layer increased. Laser surface alloying of alloys, including aluminum alloy, was studied by Kogan [4]. He demonstrated that the structure, phase, and chemical composition of the zones of hardening could be determined by the process parameters and the laser treatment of aluminum alloys allowed hardening zones with a hardening range from 500 to 800 HV at the surface. Laser treatment and retardation of fatigue crack

* Corresponding author.

E-mail address: naqeeli@kfupm.edu.sa (N. Al-Aqeeli).

growth in aluminum alloys was studied by Schnubel et al. [5]. Their findings revealed that substantial retardation of fatigue crack growth could be achieved through a laser treatment process. The plastic damage in aluminum alloy due to pulsed laser heating was investigated by Qin et al. [6]. They indicated that the plastic damage occurred in the top layer of the plate, where the residual radial stress was tensile and the magnitude of residual radial stress in the plastic damage region became significantly high when the Gaussian beam profile was used. Plastic deformation due to the laser heating of a metal plate was examined by Chen et al. [7]. They showed that the plastic zone outspread gradually and extended across the depth of the metal at high laser power intensities.

Metallurgical changes in the laser treated layer have been a research interest for improvement of surface properties including microhardness and wear resistance [8–11]. Metallurgical changes at the laser treated aluminum surface during laser shock processing were studied by Schneider et al. [8]. They modeled the growth of voids in incipient spalling by dislocation loop emission from the void surface and they proposed the first dislocation-based void growth mechanism by incorporating the three dimensional consideration. Laser cladding of Fe–Cr–C alloy on the aluminum alloy surface was carried out by Iwatani et al. [9]. They demonstrated that the number of cracks in the clad layer decreased with decreasing hardness and formation of the ferrite in the austenite phase was achieved by controlling the dilution ratio and the carbon content of the cladding material. In addition, the clad layer exhibited a higher wear resistance compared with the aluminum alloy. The microstructural changes in laser induced ceramic coatings on aluminum alloys were studied by Kadolkar and Dahotre [10]. They indicated that, by controlling the process parameters, it was possible to produce varied microstructures at the surface according to the requirements of a specific application. Microstructural study due to laser treated aluminum alloy surface was presented by Araujo et al. [11]. They demonstrated that the heat affected zone was shallow and, due to temperature range across the heat affected zone, which was in between 548 and 596 °C, α -liquid phases took place in this region during the processing.

Laser treatment alters the surface texture of the treated layer; in which case, surface hydrophobicity could change drastically. Although considerable research studies were carried out to examine the surface hydrophobicity of the aluminum alloys, only little work was reported on laser treatment and surface hydrophobicity of the aluminum alloys [12]. Aluminum has ionic metal characteristics and demonstrates some hydrophobic feature at the surface. Hydrophobic behavior of the surfaces becomes important because of the requirements of anti-sticking, anti-contamination, and self-cleaning of surfaces in practice. Surface hydrophobicity can be improved through creating surface textures at nano/micro sizes while mimicking some natural plants such as lotus leaves, rice leaves, red rose petals, fish scales, etc. [13–17]. In addition, surface free energy of the substrate material plays an important role for the surface hydrophobicity. Therefore, the surface energy can be reduced through altering chemical composition of the substrate material and forming new compounds at the surface. Although many techniques are proposed and strategies are introduced to enhance the hydrophobicity of the surfaces [18–26], not all of these techniques have the practical or cost effective applications due to the involvement of multi-step procedures and harsh conditions. However, surface texturing during laser treatment may offer less challenges with cost effective texturing, which is particularly true when high pressure nitrogen assisting gas is introduced during the processing [12]. In this case, nitride compounds can be formed at the surface while reducing to surface free energy towards increasing the surface hydrophobicity [12].

Although laser surface treatment of engineering alloys is carried out previously [27–30], surface treatment of aluminum

composite with presence of the hard particles is left for the future study. Therefore, in the present study, laser controlled melting of aluminum composite pellets is carried out. Aluminum pellets are formed from the mixture of 85% (wt) high-purity aluminum and 15% B₄C (wt) particles through the hot pressing. Laser treated surfaces are examined incorporating the analytical tools including scanning electron microscope, atomic force microscopy, energy dispersive spectroscopy, and X-ray diffraction. Microhardness and fracture toughness of the resulting surfaces are evaluated through the indentation tests. Surface hydrophobicity is assessed by the contact angle measurements. The scratch tests are carried out to determine the scratch resistance of the laser treated surface.

2. Experimental

The workpieces were formed from high-purity aluminum mixed with 15% commercial-grade B₄C powders with 99% purity. The workpieces were in a circular pellet form of 25.4 mm in diameter and 3 mm in thickness. Aluminum powders had particle size in the order of 200 μ m and B₄C powders had median size of 2 μ m. To prepare the pellets, B₄C and aluminum powders were mixed in isopropyl alcohol. The slurry was, then, ultrasonically shook to achieve homogeneity for 30 min. The pellets were compacted through sintering, hot-pressing, and hot isostatic pressing. The pellets were cold-pressed at 60 MPa, provided that the higher pressures resulted in undesirable striations in the compacts and they were sintered in a vacuum furnace at a temperature within the range of 450 °C and a pressure of 200 MPa in an environment pressure of 5×10^{-2} Pa for thirty minutes [31]. Hot isostatic pressing were performed in accordance with the maximum temperature (1100 °C) for 30 min hold at 200 MPa argon environments. Heating and cooling rates of 50 °C/min were used at 200 MPa. The pellets were furnace cooled under the vacuum conditions.

The CO₂ laser (LC-ALPHAIII) delivering a nominal output power of 2 kW was used to irradiate the workpiece surface [32]. The nominal focal length of the focusing lens was 127 mm and the diameter of the laser beam focused at the workpiece surface was \sim 0.3 mm. The laser intensity distribution at the irradiated spot is Gaussian. Nitrogen gas used as the assisting gas was applied co-axially with the laser beam using a conical nozzle and the laser treatment was repeated several times using different laser parameters. Laser parameters resulting in controlled melting of the surface with a minimum of surface defects, such as very small cavities without crack networks, were selected and the laser treatment conditions are shown in Table 1. The laser treatment is repeated several times to ensure the repeatability of the surface texture and structures. The workpiece surface was scanned by a laser through a circular orientation as shown in Fig. 1. This arrangement provides self-annealing effect of the recently formed laser tracks on the previously formed tracks.

Material characterization of the laser treated surfaces was conducted using an optical microscope, SEM, EDS, and XRD. A Jeol 6460 Scanning Electron Microscope was used for SEM examinations and a Bruker D8 Advanced X-ray Diffractometer using CuK α radiation was used for XRD analysis. Typical settings of the XRD

Table 1
Laser heating conditions used in the experiment.

Scanning speed (mm/min)	Peak power (W)	Frequency (Hz)	Nozzle gap (mm)	Nozzle diameter (mm)	Focus setting (mm)	N ₂ pressure (kPa)
600	1500	1000	1.5	1.5	127	550

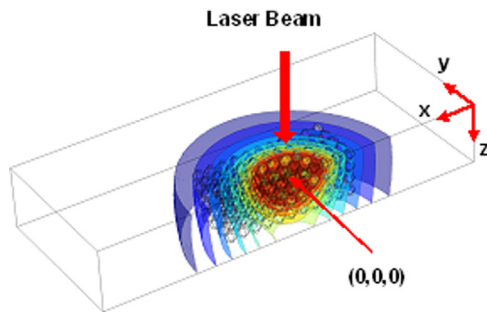


Fig. 1. Schematic view of laser scanning at the workpiece surface. Since the schematic view is shown, heating coloration is shown schematically without temperature bar.

were 40 kV and 30 mA with the scanning angle (2θ) ranging from 20° to 80° . Surface roughness measurement of the laser-melted surfaces was performed using an Agilent 5100 AFM in the contact mode. The tip was made of silicon nitride probes ($r=20\text{--}60\text{ nm}$) with a manufacturer specified force constant, k , of 0.12 N/m.

A Microphotonics digital microhardness tester (MP-100TC) was used to determine the microhardness at the surface. The standard test method for Vickers indentation hardness of advanced ceramics (ASTM C1327–99) was adopted. Microhardness was measured at the surface of the workpiece after the laser treatment process and the measurements were repeated five times at each location to determine the consistency of the results. The error estimated for the measurements is in the order of 4%.

A linear micro-scratch tester (MCTX-S/N: 01–04300) was used to determine the scratch resistance and friction coefficient of the laser treated and untreated surfaces. The equipment was set at a contact load ranging from 0.03 N to 5 N. The scanning speed was 5 mm/min with a loading rate of 5 N/s and the total length for the scratch tests was 5 mm. The scratch tests were repeated three times for consistency of the data. The error related to the friction coefficient due to the repeatability of the experiment is within 5%.

The wetting experiment was performed using a Kyowa (model – DM 501) contact angle goniometer. The static sessile drop method was adopted for the contact angle measurement. The water contact angle between a water droplet and the heat treated surface was measured with de-ionized water used as the fluid medium. Droplet volume was controlled with an automatic dispensing system having a volume step resolution of 0.1 μl . Still images were captured, and the contact angle measurements were performed with one second duration of deposition of a water droplet on the surface.

The fracture toughness of the surface was determined using the indenter test data for microhardness (Vickers) and crack inhibiting. In this case, microhardness in HV and the crack length generated due to indentation at the surface were measured. The length (l) measured corresponds to the distance from the crack tip to the indent. The crack lengths were individually summed to obtain $\sum l$ as described in a previous study [33]. The crack length “ c ” from the center of the indent was the sum of individual crack lengths ($\sum l$) and half of the diagonal length of the indent “ $2a$ ”. Therefore, $c=a+\sum l$. However, depending upon the ratio of c/a , average of equations was developed to estimate the fracture toughness (K). However, the equation proposed by Anstis et al. [34] has limitations due to nonlinearity of the coefficients for values of $c/a > 2$, which is not applicable for tungsten carbide ($\approx 2.5\text{--}4.5$). Therefore, the equation proposed by Evans and Charles [35] was used to determine the fracture toughness (K_c), which is applicable for $(0.6 \leq c/a \leq 4.5)$, i.e.,

$$K_c = 0.079 \left(\frac{P}{a}\right)^{1.5} \cdot \log \left(4.5 \frac{P}{c}\right) \quad (1)$$

where P is the applied load on indenter, c is the crack length, and a is half of the diagonal length of the indent. Table 2 shows the data used for the fracture toughness calculations.

3. Results and discussion

Laser controlled melting of aluminum based composite mixed with B_4C hard particles is carried out. Surface characteristics including metallurgical changes, surface texture, microhardness, fracture toughness, scratch resistance, and hydrophobicity are assessed after the laser treatment process.

3.1. Morphological and metallurgical changes

Fig. 2 shows optical photograph of laser treated surface while Fig. 3 shows SEM micrographs of the laser treated surface. Since the laser treatment is carried out through rotational scanning of the workpiece surface by a laser beam, laser treated area has a circular feature. In general, the laser treated surface composes of regular laser scanning tracks, which is formed through overlapping of the laser irradiated spots at the surface. It should be noted that high frequency (1500 Hz) repetitive laser pulses are used to irradiate the surface during the controlled melting. The overlapping ratio of the consecutive laser pulses is 72% at the surface, which provides continuous melting at the surface. Since the laser intensity distribution is Gaussian at the irradiated surface, the peak intensity occurs at the center of the irradiated spot. This, in turn, causes a small size local evaporation at the surface. However, the molten flow from the irradiated spot modifies the previously formed cavity at the surface; consequently, large scale cavity formation does not take place at the surface. The photo-induced nonlinear optical effects cause enhance electron–phonon harmonic behavior, which may cause heating enhancement in the irradiated surface; however, this effect is referred to [36,37]. Since surface melting is carried out under the controlled environment, no molten flow is observed across the laser scanning tracks. Although the cooling rate is high at the surface, no micro-crack or crack network is observed from the SEM micrograph. This is associated with the self-annealing effect of the lately formed laser tracks on the previously formed tracks. In this case, heat conduction from the lately formed tracks towards the initially formed tracks modifies the cooling rates in the surface vicinity. In addition, laser controlled melting modifies the structure at the surface; in this case, fine grains are formed after the re-solidification and after close examination of several SEM images, the grain size is estimated in the order of 0.8–0.4 μm . Since the surface temperature remains below the melting temperature of B_4C , hard particles remain in solid phase during the laser melting process. It should be noted that the melting temperature of B_4C (2645 K [38]), which is higher than the melting temperature of the aluminum alloy (933 K [37]). Grain refinement at the surface results in volume shrinkage and dense layer formation in the surface region of the laser treated layer. Although thermal expansion coefficients of B_4C ($5 \times 10^{-6} \text{ } 1/^\circ\text{C}$ [39]) and aluminum ($22.2 \times 10^{-6} \text{ } 1/^\circ\text{C}$ [40]) are different, no micro-cracks are observed around the hard particles after the re-solidification of the surface, which is associated with the self-annealing effect of the lately formed laser scanning tracks

Table 2
Fracture toughness and data used for fracture toughness calculations.

	P (N)	a (μm)	c (μm)
As-received Surface	5	30	5
Laser treated Surface	5	20	50

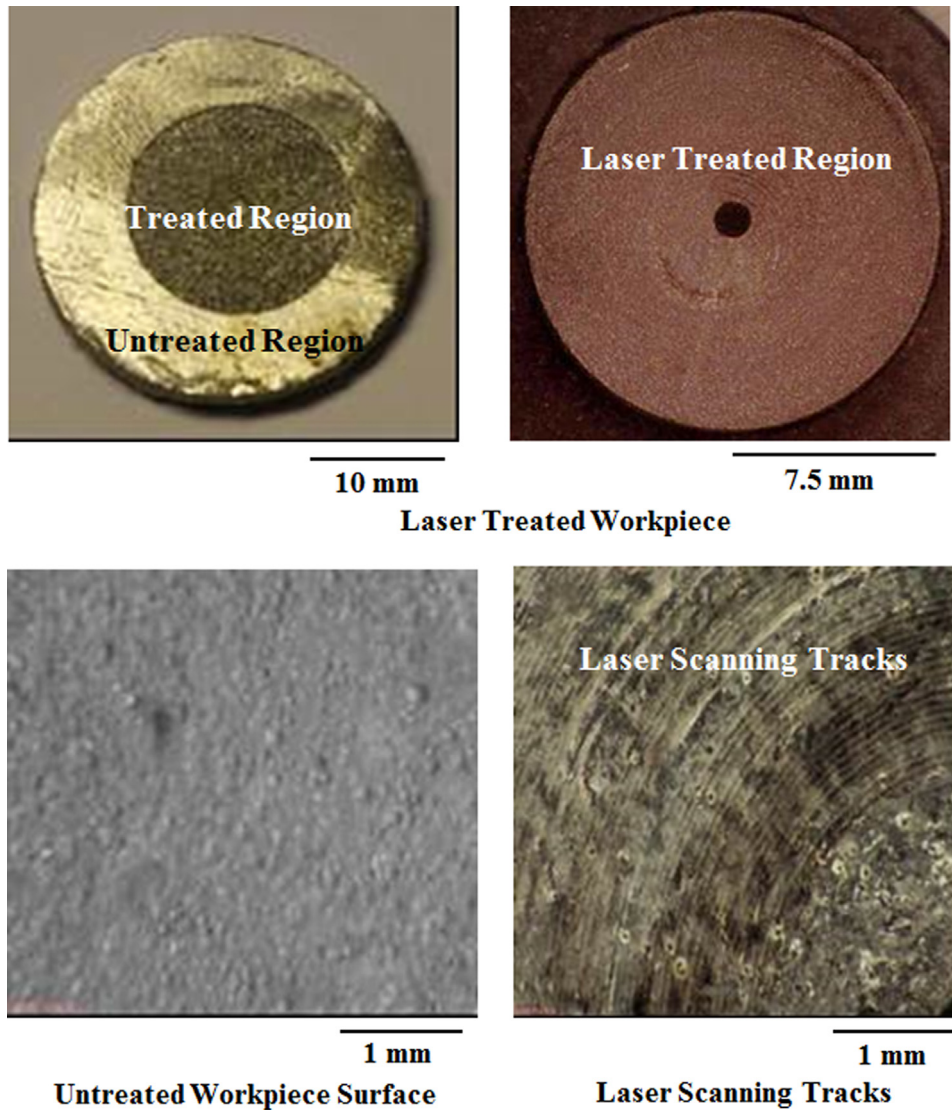


Fig. 2. Optical images of laser treated and untreated workpiece surfaces.

on the initially formed tracks. Therefore, micro-stresses formed in the near region of the hard particles are modified through the self-annealing effect of the lately formed laser tracks.

Fig. 4 shows the SEM micrographs of the cross-section of the laser treated layer. The laser treated layer extends uniformly about $40\ \mu\text{m}$ below the surface, which is free from the large scale asperities such as large scale cracks and voids. The dense layer is formed at the surface, which consists of fine grains and the hard particles. The close examination of SEM micrographs reveals that no voids or micro-cracks are formed in the close region of the hard particles. Although the surface texture of the hard particles possesses hydrophobicity, the slow rate of solidification suppresses the void formation around the hard particles. Consequently, self-annealing effect generated, due to circular scanning of the laser beam at the surface, suppresses the solidification rate in the laser treated layer. The use of high pressure nitrogen as an assisting gas results in formation of AlN compound at the surface, which can be observed from the X-ray diffractogram of the laser treated surface as shown in Fig. 5. In the region next to the dense layer, dark inclusions are observed. This is associated with the grain structure persisting in α -liquid region, which indicates incomplete reach of liquid phase in this region [11]. As the depth below the surface increases, small size cellular structure is

observed, which typically appears in cast aluminum alloys [41]. The dendritic structures are formed in the region close to the heat affected zone because of the relatively higher cooling rates than that corresponding to the heat affected zone. In this case, rapid quenching is responsible for the formation of the dendritic structures in the interfacial region of the heat affected zone. As the depth below the surface increases further, grain size increases demonstrating the presence of the heat affected zone. Table 3 shows EDS data obtained for different locations at the laser treated surface. The elemental composition remains almost uniform at the laser treated surface. Although the quantification of light elements are difficult from the EDS data, presence of nitrogen is evident. This indicates the nitride compound formation at the surface, which is in agreement with the X-ray diffractogram (Fig. 5).

3.2. Microhardness, fracture toughness, and scratch resistance

Table 4 shows microhardness and fracture toughness of the laser treated and untreated surfaces. Microhardness increases significantly after the laser treatment process. This is attributed to one or all of the followings: (i) formation of the dense layer in the surface region due to the high cooling rates, (ii) AlN compound

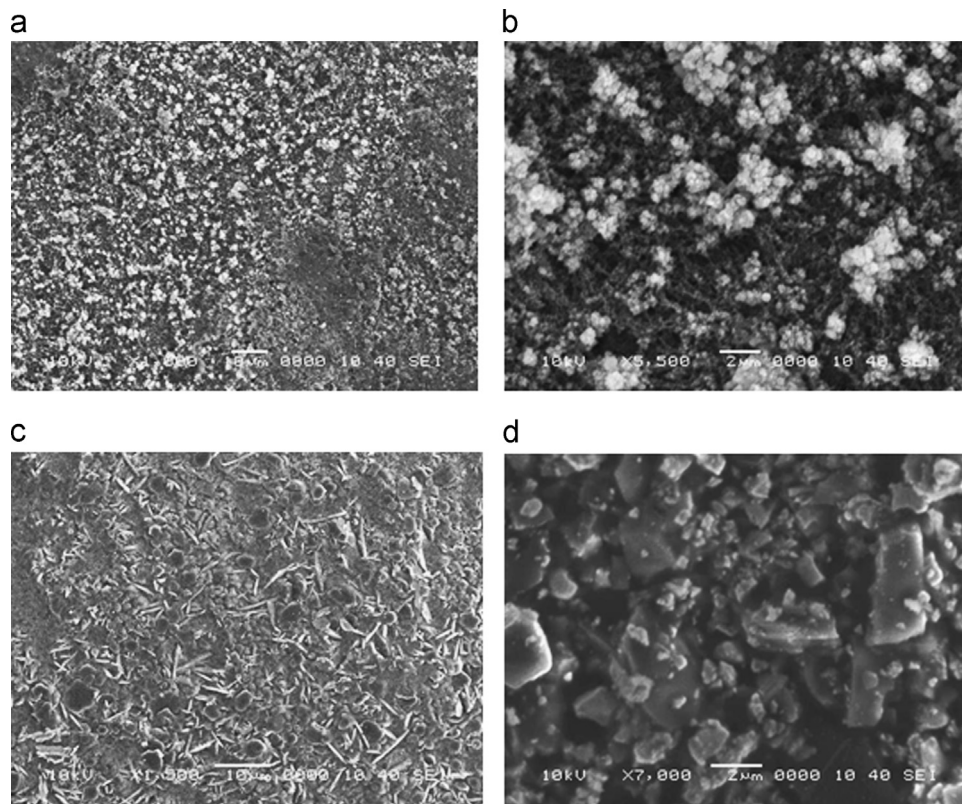


Fig. 3. SEM micrographs of laser treated and untreated surfaces: (a) Laser treated surface and texture, (b) Laser treated surface and fine structures, (c) Untreated surface and texture, (d) Untreated surface and hard particles (B_4C).

formation at the surface because of the high pressure nitrogen assisting gas, and (iii) micro-stresses formed around the hard particles because of the mismatch of the thermal expansion coefficients between B_4C and aluminum. It should be noted that microhardness measurements are repeated five times at different locations on the surface. The experimental error based on the repeatability of microhardness data is in the order of 8%. The variation of microhardness across the laser treated surface can be explained in terms of: (i) the non-uniform distribution of B_4C particles at the surface, (ii) non-uniform cooling of the surface during the laser scanning, and (iii) non-uniform distribution of AlN compounds. Fracture toughness of the surface reduces slightly after the laser treatment process. This can be related to the dense layer formation at the surface, which enhances microhardness and lowers the fracture toughness. In addition, the micro-stresses formed in the region of B_4C particles contribute to the fracture toughness reduction at the surface. The fracture failure normally takes place at the surface under tension; however it can also occur due to surface compressive stresses when the crack tip exceeds the sum of theoretical strength. The percentage difference of the fracture toughness between the laser treated surface and the untreated surface is about 12%.

Fig. 6 shows the scratch test results used to determine the friction coefficient of the laser treated and untreated surfaces while Fig. 7 shows the scar marks resulting from the scratch tests for laser treated and untreated surfaces. The laser treated surface results in lower friction coefficient than that corresponding to the untreated surface, the reduction in the friction coefficient is attributed to the low surface roughness and high hardness of the laser treated surface. The optical image for the scratched marks shows that the scar size remains almost uniform along the tested surface and the depth of the scar marks is considerably shallow for the laser treated surface. However, the presence of hard particles alters the scar depth and the scar marks at the surface; in which

case, scar depth reduces and scar size becomes narrow at the surface. This observation is also valid for untreated workpiece surface.

3.3. Surface hydrophobicity

Fig. 8 shows images of atomic force microscope for the laser treated surface. The laser treated surface has the texture composing of micro/nano poles. The average surface roughness is in between 0.4 and 0.7 μm . The presence of micro poles can be associated with the small scale ablation of the surface and the presence of the hard particles, which can also be observed from Fig. 4, in which SEM image of the laser treated surface is shown. In addition, sub-micron size and closely spaced fiber like texture is also evident from the image of the atomic force microscope. On the other hand, the hydrophobicity of the laser treated and untreated surfaces can be assessed through measuring the contact angle of the water droplet; in which case, the contact angle of the water droplet on a perfectly smooth and chemically homogenous solid surface can be written in terms of Young's equation [42]:

$$\cos\theta = \frac{(\gamma_{sv} - \gamma_{sl})}{\gamma_{lv}} \quad (2)$$

where θ is the contact angle, γ_{sv} is the interfacial tension of the solid-vapor interface, γ_{sl} is the interfacial tension of the solid-liquid interface, and γ_{lv} is the interfacial tension of liquid-vapor interface. However, the practical application of Young's equation is limited because of the non-uniform surface texture and chemically heterogeneous structures formed at the surface. Wenzel [43] and Cassie and Baxter [44] proposed an equation including the roughness factor to overcome this limitation. Wenzel formulation incorporates the liquid penetration into the rough texture and

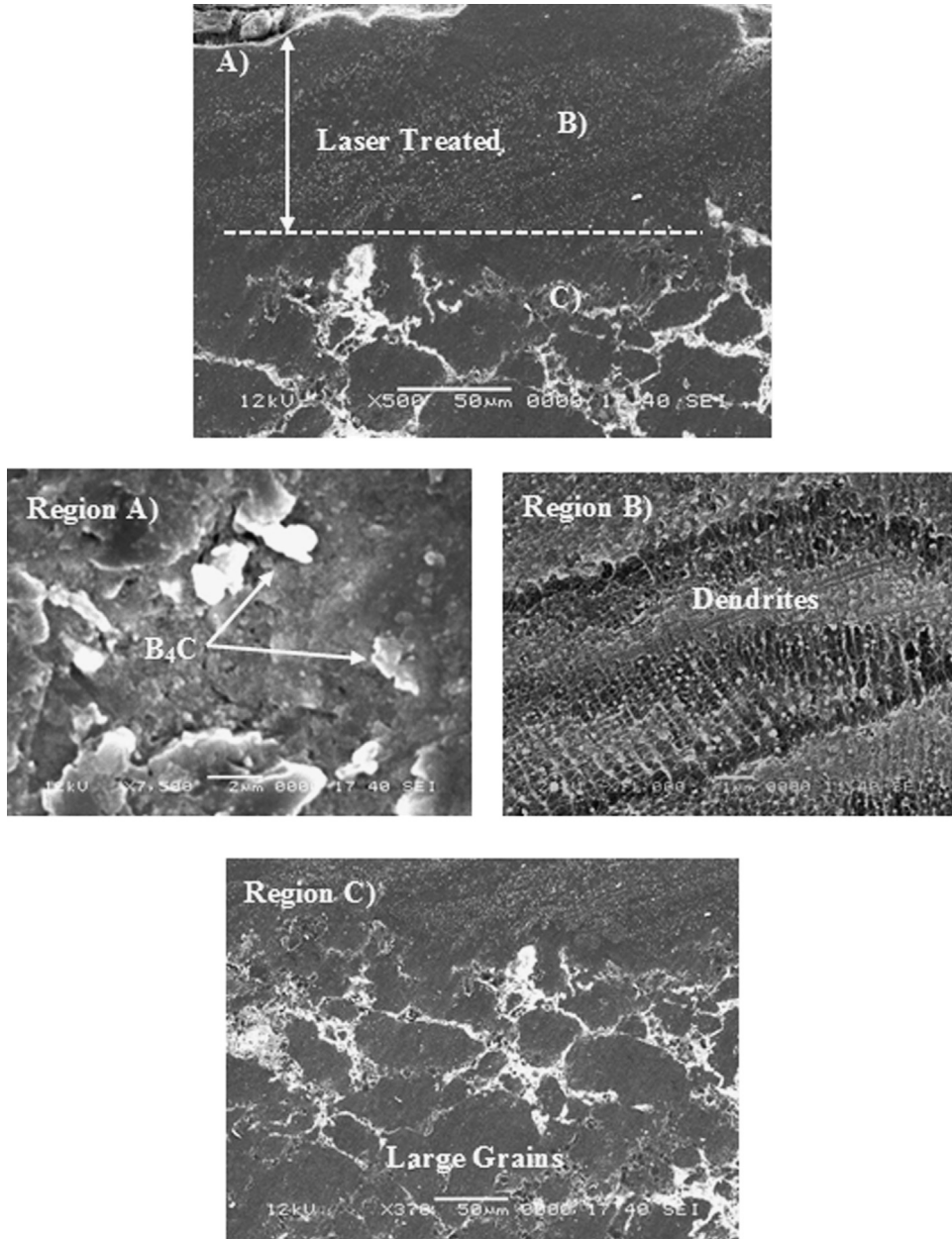


Fig. 4. SEM micrograph of cross-section of laser treated region with specific regions: (A) Fine grains with B₄C particles, (B) Dendritic structures, and (C) Heat affected zone.

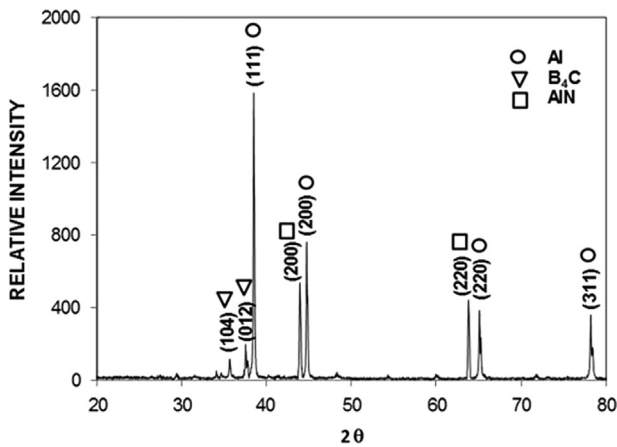


Fig. 5. X-ray diffractogram of laser treated surface.

Table 3

Elemental composition of laser treated surface obtained from EDS data (wt%). Spectrum corresponds to a location at the surface and EDS data represent weight percentile of constituting elements.

Spectrum	N	B	O	Al
Spectrum 1	5.3	15.1	4.2	Balance
Spectrum 2	6.4	14.7	2.4	Balance
Spectrum 3	6.5	14.9	3.2	Balance
Spectrum 4	5.9	15.3	3.1	Balance

expresses the contact angle as follows [43]:

$$\cos\theta_w = \frac{r(\gamma_{sv} - \gamma_{sl})}{\gamma_{lv}} \quad (3)$$

where θ_w is the rough surface contact angle, and r is the surface roughness factor, which is defined as the ratio between the actual and projected surface areas, where $r=1$ for a perfectly smooth

surface and $r > 1$ for a rough surface. However, the interface of the liquid droplet composes of liquid–solid and liquid–vapor interfaces and the contact angle of both interfaces needs to be considered in the contact angle formulation. The contact angle formulation, therefore, can be expressed as [44,45]:

$$\cos\theta_c = f_1 \cos\theta_1 + f_2 \cos\theta_2 \tag{4}$$

where θ_c is the apparent contact angle, f_1 is the surface fraction of the liquid–solid interface, f_2 is the surface fraction of the liquid–vapor interface, θ_1 is the contact angle of the liquid–solid interface, and θ_2 is the contact angle for liquid–vapor interface. In the case of an air–liquid interface, the air fraction (f_2) becomes $(1 - f_1)$. For $f_1 = 0$, the liquid droplet is not in contact with the solid surface and for $f_1 = 1$, the droplet completely wets the surface. The optical image of the water droplet used for the contact angle measurement is shown in Fig. 9 for laser treated and untreated surfaces while Table 5 shows the contact angles measured at the laser treated and untreated surfaces. The values of the contact angle changes at different locations at the surface, which is related to the surface roughness variation and the different texture compositions across the laser treated surface as consistent with the previous study [12]. However, the water droplet remains in a Wenzel state at the rough surface; in which case, the contact angle remain low, as observed from the optical photograph (Fig. 9). Consequently, the water droplet penetrates through the surface texture having the large pole heights and large pole spacing. This situation occurs only twice out of ten tests at the surface. The contact angle remains higher for the laser treated surface than that of the untreated surface. This is associated with the laser induced texturing of the surface and the presence of AlN compound at the surface, which is formed during the laser treatment process. In this case, the surface free energy of AlN is 38.3 mJ/m^2 [46] when compared to 93.9 mJ/m^2 for Al [47]. The low surface energy of AlN (γ_{sl}) enhances the contact angle for the laser treated surface. In addition, the fine texture with nano/micro poles promotes the presence of air pockets in between the water droplet and the surface. Consequently, the Cassie and Baxter state, mainly, occurs

at the laser treated surface; therefore, f in Eq. (4) remains low for large contact angles. Hence, laser treatment provides the surface texture consisting of fine size poles with narrow widths of micro/nano sizes. Although Wenzel state occurs across some regions of the laser treated surface, the Cassie and Baxter state covers a larger area at the surface than that corresponding to the Wenzel state.

4. Conclusions

Laser treatment of hot pressed aluminum (85 wt%) and B₄C (15 wt%) composite surface is carried out. Morphological and metallurgical changes at the laser treated surface are examined using electron scanning and optical microscopy, energy dispersive spectroscopy, and X-ray diffraction. Hardness and fracture toughness of the laser treated surface are determined using the indentation tests. Surface texture and hydrophobicity of the laser treated surface is assessed incorporating the atomic force microscopy and contact angle measurements. It is found that the laser treated surface composes of laser scanning tracks with circular geometric orientation. The overlapping ratio of the laser irradiated spots at the surface is in the order of 72%, which provides continuous melting at the surface. Laser treated surface is free from large scale asperities such as large cracks and cavities. Since the laser beam intensity is Gaussian across the irradiated spot, small scale local evaporation takes place at the irradiated surface. This results in a surface texture composing of micro/nano size

Table 4
Microhardness and fracture toughness at the workpiece surface prior to and after the laser treatment process.

	Hardness (HV)	Fracture toughness ($\text{MPa}\sqrt{\text{m}}$)
As received surface	220 (+10/−10)	11.5 ± 0.2
Laser treated surface	900 (+20/−20)	9.5 ± 0.4

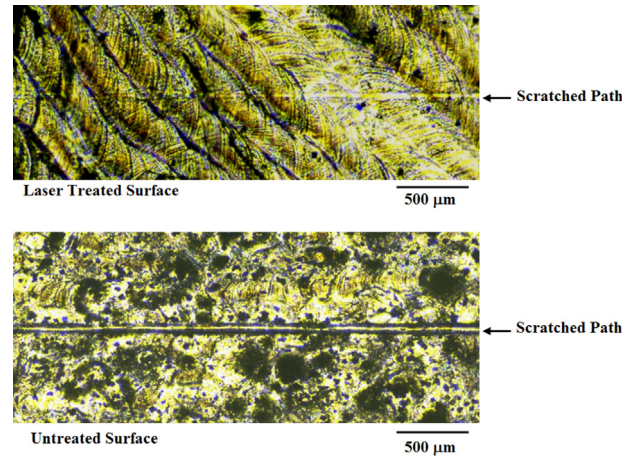


Fig. 7. Images of scratch marks on laser treated and untreated surfaces.

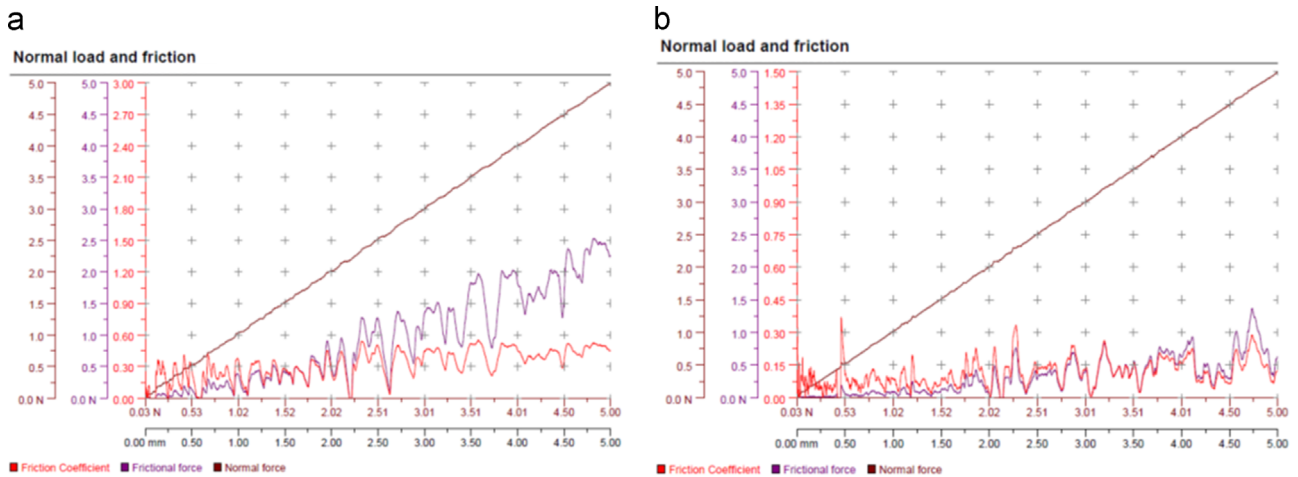


Fig. 6. Scratch test results for: (a) Untreated workpiece surface, and (b) Laser treated surface.

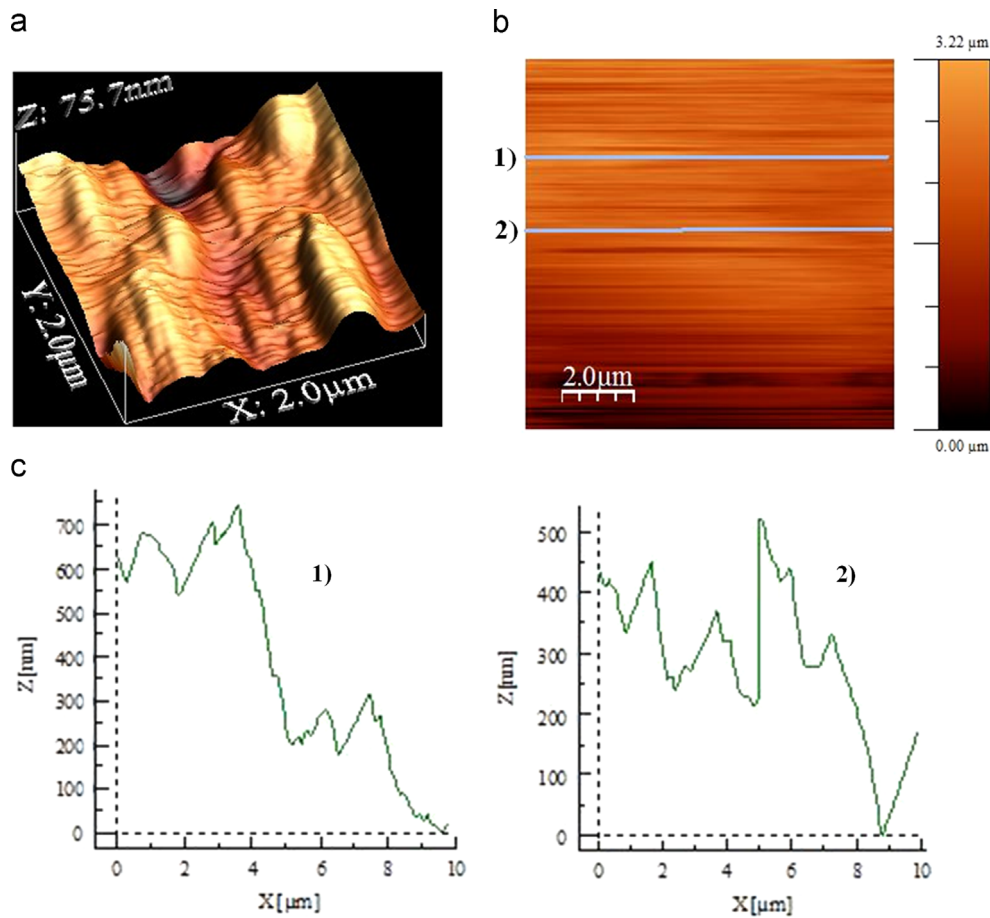


Fig. 8. FAM images of the laser treated surface: (a) Three-dimensional view of texture, (b) Image for surface roughness measurement, and (c) Surface roughness along the line (1) and (2).

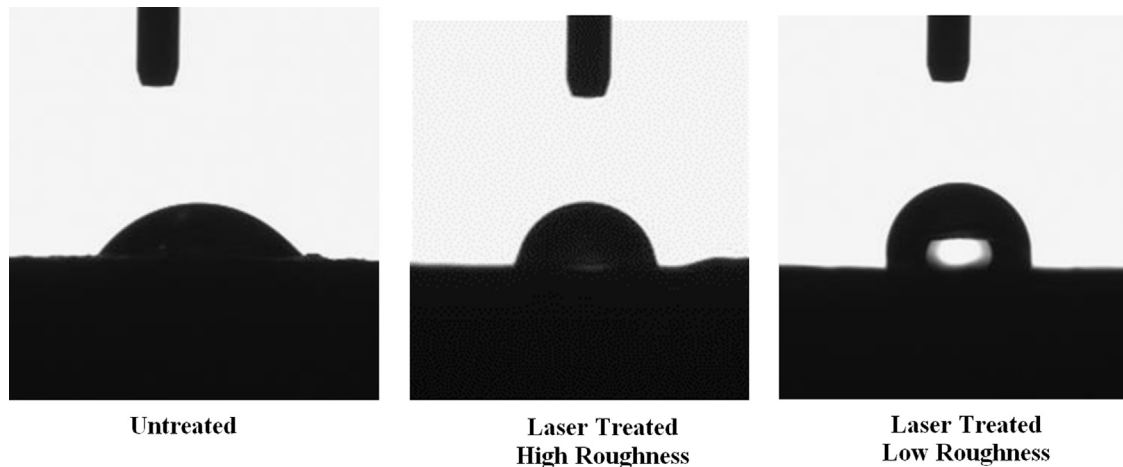


Fig. 9. Images used for contact angle measurements.

Table 5
Contact angles measurement results prior to and after the laser treatment.

	Contact angle (deg.)	
	Low roughness	High roughness
Laser treated surface	124.2 (+5/−5)	86.1 (+5/−5)
Untreated surface	63.5 (+5/−5)	

poles. The self-annealing effect of the lately formed laser tracks alters the cooling rates at the surface; in which case, micro-crack or crack-network formation is avoided at the laser treated surface. A dense layer consisting of fine grains and B_4C particles is formed at the laser treated surface. Although thermal expansion coefficients of aluminum and B_4C particles are different, no micro-cracks or crack-network is observed in the dense layer. In addition, no void appears around the hard particles because of the volume shrinkage in the dense layer. The dendritic structures are formed

in the region below the dense layer and the size of the dendrites increases in the near region of the heat affected zone. The grain size enlargement takes place in the heat affected zone due to the low cooling rates in this region. Microhardness increases at the laser treated surface because of the presence of the dense layer and the formation of AlN compounds at the surface. However, fracture toughness reduces slightly because of the microhardness enhancement at the surface. The laser treated surface results in lower friction coefficient than that of the untreated surface, which is attributed to the low surface roughness and high hardness of the laser treated surface. In addition, the scratched marks remain almost uniform along the tested surface and the depth of the scar marks is considerably shallow for the laser treated surface. The laser treated surface texture composes of micro/nano size poles, which influence the surface hydrophobicity of the laser treated workpieces. In this case, laser treated surface results in larger contact angles than that of the untreated surface. This is associated with the surface texture and formation of AlN compounds, which has low surface energy than aluminum.

Acknowledgments

The authors acknowledge the financial support of King Fahd University of Petroleum and Minerals (KFUPM) through Project# MIT11111-11112, and King Abdulaziz City for Science and Technology (KACST) through Project# 11-ADV2134-04 to accomplish this work.

References

- [1] Halverson DC, Pyzik AJ, Aksay IA, Snowden WE. Processing of boron carbide–aluminum composites. *J Am Ceram Soc* 1989;72(5):775–80.
- [2] Zhang Z, Fortin K, Charette A, Chen X-G. Fluidity and microstructure evolution of al-12%b4c composites containing magnesium. *Mater Trans* 2011;52(5):928–33.
- [3] Pokhmurs'ka HV. Structural changes in the surface layer of D16 alloy clad with aluminum in the process of laser heating. *Mater Sci* 2002;38(6):889–93.
- [4] Kogan Y. Theory and technology of surface alloying of iron, aluminum, copper and titanium with laser heating. *ASM Proc: Heat Treat* 2000;1:165–9.
- [5] Schnubel D, Horstmann M, Ventzke V, Riekehr S, Staron P, Fischer T, et al. Retardation of fatigue crack growth in aircraft aluminum alloys via laser heating - Experimental proof of concept. *Mater Sci Eng A* 2012;546:8–14.
- [6] Qin Y, Chen Y, Ni X, Shen Z, Bi J, Zhang X. Axisymmetric numerical simulation of plastic damage in aluminum alloy induced by long pulsed laser. *Opt Lasers Eng* 2010;48(3):361–7.
- [7] Chen Y, Lu J, Ni X, Bi J, Zhang X. Plastic penetration during laser heating of a metal plate. *Source: J Mater Process Technol* 2008;205(1–3):9–15.
- [8] Schneider MS, Kad B, Kalantar DH, Remington BA, Kenik E, Jarmakani H, et al. Laser shock compression of copper and copper-aluminum alloys. *Int J Impact Eng* 2006;32(1–4):473–507.
- [9] Iwatani S, Ogata Y, Uenishi K, Kobayashi KF, Tsuboi A. Laser cladding of Fe–Cr–C alloys on A5052 aluminum alloy using diode laser. *Mater Trans* 2005;46(6):1341–7.
- [10] Kadolkar P, Dahotre NB. Variation of structure with input energy during laser surface engineering of ceramic coatings on aluminum alloys. *Appl Surf Sci* 2002;199(1–4):222–33.
- [11] Araujo D, Carpio FJ, Mendez D, Garcia AJ, Villar MP, Garcia R, et al. Microstructural study of CO₂ laser machined heat affected zone of 2024 aluminum alloy. *Appl Surf Sci* 2003;208–209(1):210–7.
- [12] Yilbas BS, Khaled M, Abu-Dheir N, Al-Aqeeli N, Furquan SZ. Laser texturing of alumina surface for improved hydrophobicity. *Appl Surf Sci* 2013;286:161–70.
- [13] Wagner T, Neinhuis C, Barthlott W. Wettability and contaminability of insect wings as a function of their surface sculptures. *Acta Zool* 1996;77(3):213–25.
- [14] Parker AR, Lawrence CR. Water capture from desert fogs by a namibian beetle. *Nature* 2001;414(6859):33–4.
- [15] Gao X, Jiang L. Biophysics: water-repellent legs of water striders. *Nature* 2004;432(7013):36.
- [16] Byun D, Hong J, Saputra JH, Ko YJ, Lee HC, Park BK, et al. Wetting characteristics of insect wing surfaces. *J Bionic Eng* 2009;6(1):63–70.
- [17] Koch K, Bhushan B, Barthlott W. Diversity of structure, morphology and wetting of plant surfaces. *Soft Matter* 2008;4(10):1943–63.
- [18] Han JT, Xu XR, Cho KW. Diverse access to artificial superhydrophobic surfaces using block co- polymers. *Langmuir* 2005;21(15):6662–5.
- [19] Shirtcliffe NJ, McHale G, Newton MI, Chabrol G, Perry CC. Dual-scale roughness produces unusually water-repellent surfaces. *Adv Mater* 2004;16(21):1929–32.
- [20] Hwang HS, Lee SB, Park I. Fabrication of rasp- berry-like superhydrophobic hollow silica particles. *Mater Lett* 2010;64(20):2159–62.
- [21] Huang YH, Wu JT, Yang SY. Direct fabricating patterns using stamping transfer process with pdms mold of hydrophobic nanostructures on surface of micro cavity. *Microelectron Eng* 2011;88(6):849–54.
- [22] Yang T, Tian H, Chen Y. Preparation of superhydrophobic silica films with honeycomb-like structure by emulsion method. *J Sol–Gel Sci Technol* 2009;49(2):243–6.
- [23] Kinoshita H, Ogasahara A, Fukuda Y, Ohmae N. Superhydrophobic/superhydrophilic micropatterning on a carbon nanotube film using a laser plasma-type hyperthermal atom beam facility. *Carbon* 2010;48(15):4403–8.
- [24] Latthe SS, Imai H, Ganesan V, Rao AV. Super- hydrophobic silica films by sol-gel co-precursor method. *Appl Surf Sci* 2009;256(1):217–22.
- [25] Ma M, Mao Y, Gupta M, Gleason KK, Rutledge GC. Superhydrophobic fabrics produced by electrospinning and chemical vapor deposition. *Macromolecules* 2005;38(23):9742–8.
- [26] Zhang X, Guo Y, Zhang P, Wu Z, Zhang Z. Superhydrophobic CuO/Cu₂S nanoplate vertical arrays on copper surfaces. *Mater Lett* 2010;64(10):1200–3.
- [27] Yilbas BS, Akhtar SS, Karatas C. Laser gas assisted melting of pre-prepared alumina surface including TiC particles at surface. *Surf Eng* 2011;27:470–6.
- [28] Yilbas BS. Characterization of laser treated Rene 41 surface due to B₄C and SiC particles at surface prior to laser treatment. *Surf Interface Anal* 2014;46:30–5.
- [29] Yilbas BS, Akhtar SS, Karatas C. Laser carbonitriding of alumina surface. *Opt Lasers Eng* 2011;49:341–50.
- [30] Yilbas BS, Al-Aqeeli N, Karatas C. Laser control melting of alumina surfaces with presence of B₄C particles. *J Alloys Compd* 2012;539:12–6.
- [31] Tanerolu H, Akar N, Kiliçi V. Examination of microstructure and mechanical properties of Al2024 alloy produced by thixocasting. *J Fac Eng Archit Gazi Univ* 2013;28(4):803–9.
- [32] (<http://www.amada.com/america/>) 2014.
- [33] Lopez Cantera E, Mellor BG. Fracture toughness and crack morphologies in eroded WC–Co–Cr thermally sprayed coatings. *Mater Lett* 1998;37:201–10.
- [34] Anstis GR, Chantikul P, Lawn BR, Marshall DB. A critical evaluation of indentation techniques for measuring fracture toughness: I, direct crack measurements. *J Am Ceram Soc* 1981;64:533–8.
- [35] Evans AG, Charles EA. Fracture toughness determinations by indentation. *J Am Ceram Soc* 1976;59:370–1.
- [36] Domnich V, Reynaud S, Haber RA, Chhowalla M. Boron carbide: structure, properties, and stability under stress. *J Am Ceram Soc* 2011;94(11):3605–28.
- [37] Gruhn W, Kityk IV, Benet S. Photoinduced optical second harmonic generation in Fe–Co metallic glasses. *Mater Lett* 2002;55(3):158–64.
- [38] (http://www.engineeringtoolbox.com/melting-temperature-metals-d_860.html) 2014.
- [39] (<http://www.azom.com/article.aspx?ArticleID=75>) 2014.
- [40] (http://www.engineeringtoolbox.com/linear-expansion-coefficients-d_95.html) 2014.
- [41] Uhlenbusch J, Bielech U, Klein S, Napp M, Schaefer JH. Recent developments in metal processing with pulsed laser technology. *Appl Surf Sci* 1996;106:228–34.
- [42] Neumann AW, Good RJ. In: Good RJ, Stromberg RR, editors. *Surface and Colloid Science*, II. New York: Plenum Press; 1979.
- [43] Wenzel RN. Resistance of solid surfaces to wetting by water. *Ind Eng Chemistry* 1936;28(8):988–94.
- [44] Cassie ABD, Baxter S. Wettability of porous surfaces. *Trans Faraday Soc* 1944;40:546–51.
- [45] Anand S, Paxson AT, Dhiman R, Smith JD, Varanasi KK. Enhanced condensation on lubricant-impregnated nanotextured surfaces. *ACS Nano* 2012;6(11):10122–9.
- [46] Zan H-W, Yen K-H, Liu P-K, Ku K-H, Chen C-H, Hwang J. Low-voltage organic thin film transistors with hydrophobic aluminum nitride film as gate insulator. *Org Electron* 2007;8:450–4.
- [47] Kuznetson VM, Kadyrov RI, Rudenskii GE. Calculation of surface energy of metals and alloys by the electron density functional method. *J Mater Sci Technol* 1998;14:320–2.